Ab Initio Nuclear Thermodynamics

Bing-Nan Lu,[1] Ning Li,[1] Serdar Elhatisari,[2] Dean Lee,[1] Joaquín E. Drut,[3] Timo A. Lähde,[4] Evgeny Epelbaum,[5] and Ulf-G. Meißner[6,4,7]

[1]*Facility for Rare Isotope Beams and Department of Physics and Astronomy, Michigan State University, East Lansing, Michigan 48824, USA*

[2]*Faculty of Engineering, Karamanoglu Mehmetbey University, Karaman 70100, Turkey*

[3]*Department of Physics and Astronomy, University of North Carolina, Chapel Hill, North Carolina 27599-3255, USA*

[4]*Institute for Advanced Simulation, Institut für Kernphysik, and Jülich Center for Hadron Physics, Forschungszentrum Jülich, D-52425 Jülich, Germany*

[5]*Ruhr-Universität Bochum, Fakultät für Physik und Astronomie, Institut für Theoretische Physik II, D-44780 Bochum, Germany*

[6]*Helmholtz-Institut für Strahlen- und Kernphysik and Bethe Center for Theoretical Physics, Universität Bonn, D-53115 Bonn, Germany*

[7]*Tbilisi State University, 0186 Tbilisi, Georgia*

(Received 11 April 2020; revised 6 August 2020; accepted 29 September 2020; published 3 November 2020)

We propose a new Monte Carlo method called the pinhole trace algorithm for *ab initio* calculations of the thermodynamics of nuclear systems. For typical simulations of interest, the computational speedup relative to conventional grand-canonical ensemble calculations can be as large as a factor of one thousand. Using a leading-order effective interaction that reproduces the properties of many atomic nuclei and neutron matter to a few percent accuracy, we determine the location of the critical point and the liquid-vapor coexistence line for symmetric nuclear matter with equal numbers of protons and neutrons. We also present the first *ab initio* study of the density and temperature dependence of nuclear clustering.

DOI: 10.1103/PhysRevLett.125.192502

In recent years much progress has been made in *ab initio* or fully microscopic calculations of the structure of atomic nuclei [1–6]. These first principles calculations are based on chiral effective field theory, whereby nuclear interactions are included term by term in order of importance [7]. Unfortunately, most *ab initio* methods rely on computational strategies that are not designed for calculations at nonzero temperature. One exception is many-body perturbation theory where diagrammatic expansions are used to calculate bulk thermodynamic properties [8,9]. Another exception is the method of self-consistent Green's functions, which provides nonperturbative solutions of the finite temperature system [10–13]. As with most first principles methods, however, these approaches have difficulties describing cluster correlations, which is an important feature of nuclear multifragmentation and the phase diagram of nuclear matter.

Yet another exception, which we focus on here, is the method of lattice effective field theory. Lattice effective field theory has the advantage that nonperturbative effects such as clustering are reproduced automatically when using Monte Carlo simulations. Early efforts to describe nuclear thermodynamics using lattice simulations exist in the literature [14,15], but there has been little progress since then. The difficulties stem from the computational cost of performing grand-canonical calculations of nucleons in large spatial volumes. One can reduce the effort by working in a restricted single-particle space [16,17]. Fully unbiased calculations, however, require a great amount of effort as they use matrices of size $4V \times 4V$, where V is the spatial lattice volume. In this Letter, we report a new paradigm for calculating *ab initio* nuclear thermodynamics, which we call the pinhole trace algorithm. In this algorithm, the matrices are much smaller, namely of size $A \times A$, where A is the number of nucleons. The resulting computational acceleration can be as large as a factor of one thousand.

The *ab initio* calculations presented here use the pinhole trace algorithm to implement nuclear lattice effective field theory [18,19] at finite temperature. At fixed nucleon number A, and temperature T, the expectation value of any observable $\mathcal{O}$ is

$$\langle \mathcal{O} \rangle_\beta = \frac{Z_{\mathcal{O}}(\beta)}{Z(\beta)} = \frac{\mathrm{Tr}_A(e^{-\beta H}\mathcal{O})}{\mathrm{Tr}_A(e^{-\beta H})}, \tag{1}$$

where $Z(\beta)$ is the canonical partition function, $\beta = T^{-1}$ is the inverse temperature, H is the Hamiltonian, and Tr_A is the trace over the A-nucleon states. Throughout, we use units where $\hbar = c = k_B = 1$.

The canonical partition function $Z(\beta)$ can be written explicitly in the single-particle basis as

$$Z(\beta) = \sum_{c_1,\ldots,c_A} \langle c_1, \ldots, c_A | \exp(-\beta H) | c_1, \ldots, c_A \rangle, \tag{2}$$

where the basis states are Slater determinants composed of point particles, $c_i = (\boldsymbol{n}_i, \sigma_i, \tau_i)$ are the quantum numbers of

 © 2020 American Physical Society

the ith particle, with $\boldsymbol{n}_i$ an integer triplet specifying the lattice coordinate, σ_i is the spin, and τ_i is the isospin. On the lattice, the components of $\boldsymbol{n}_i$ take integer values from 0 to $L-1$, where L is the box length in units of the lattice spacing. The neutron number N and proton number Z are separately conserved, and the summation in Eq. (2) is limited to the subspace with the specified values for N and Z.

In Supplemental Material [20] we present the full details of the lattice calculations. To explain the basic design of our computational approach, we illustrate here a simplified calculation where the Hamiltonian has a two-body contact interaction

$$H = H_{\text{free}} + \frac{1}{2}C\sum_{\boldsymbol{n}} :\rho^2(\boldsymbol{n}):, \tag{3}$$

where H_{free} is the free nucleon Hamiltonian with nucleon mass $m = 938.9$ MeV, $\rho(\boldsymbol{n}) = \sum_{\sigma,\tau} \hat{a}^\dagger_{\boldsymbol{n},\sigma,\tau}\hat{a}_{\boldsymbol{n},\sigma,\tau}$ is the density operator. The $::$ symbols indicate normal ordering where the annihilation operators are on the right and creation operators are on the left. We assume an attractive interaction with $C < 0$.

The imaginary time direction, whose length is set by the inverse temperature β, is divided into L_t slices with time lattice spacing a_t such that $\beta = L_t a_t$. For each time slice the two-body interaction is decomposed using an auxiliary-field transformation such that at each lattice site we have

$$\exp\left(-\frac{a_t C}{2}\rho^2\right) = \sqrt{\frac{1}{2\pi}}\int ds \exp\left(-\frac{s^2}{2} + \sqrt{-a_t C}s\rho\right), \tag{4}$$

where s is the auxiliary field.

Putting these pieces together, we obtain the (auxiliary-field) path-integral expression for Eq. (2)

$$Z(\beta) = \sum_{c_1,\ldots,c_A}\int \mathcal{D}s_1\cdots\mathcal{D}s_{L_t}\langle c_1,\ldots,c_A| \times M(s_{L_t})\cdots M(s_1)|c_1,\ldots,c_A\rangle, \tag{5}$$

where

$$M(s_{n_t}) =: \exp\left[-a_t K + \sqrt{-a_t C}\sum_{\boldsymbol{n}} s_{n_t}(\boldsymbol{n})\rho(\boldsymbol{n})\right]: \tag{6}$$

is the normal-ordered transfer matrix for time step n_t, and s_{n_t} is our shorthand for all auxiliary fields at that time step [18,19]. $K = -\nabla^2/2M$ is the kinetic energy operator, which is discretized using finite difference formulae [18]. For a given configuration s_{n_t}, the transfer matrix $M(s_{n_t})$ consists of a string of one-body operators which are directly applied to each single-particle wave function in the Slater determinant. For notational convenience, we will use the abbreviations $\vec{c} = \{c_1,\ldots,c_A\}$ and $\vec{s} = \{s_1,\ldots,s_{L_t}\}$.

The pinhole trace algorithm (PTA) was inspired by the pinhole algorithm used to sample the spatial positions and spin-isospin of the nucleons [38]. However, the purpose, implementation, and underlying physics of the PTA for nuclear thermodynamics are vastly different from the original pinhole algorithm used for density distributions. In the PTA we evaluate Eq. (5) using Monte Carlo methods, i.e., importance sampling is used to generate an ensemble Ω of $\{\vec{s},\vec{c}\}$ of configurations according to the relative probability distribution

$$P(\vec{s},\vec{c}) = |\langle\vec{c}|M(s_{L_t})\cdots M(s_1)|\vec{c}\rangle|. \tag{7}$$

The expectation value of any operator $\hat{O}$ can be expressed as

$$\langle\hat{O}\rangle = \langle\mathcal{M}_O(\vec{s},\vec{c})\rangle_\Omega/\langle\mathcal{M}_1(\vec{s},\vec{c})\rangle_\Omega, \tag{8}$$

where

$$\mathcal{M}_O(\vec{s},\vec{c}) = \langle\vec{c}|M(s_{L_t})\cdots M(s_{L_t/2+1})\hat{O} \times M(s_{L_t/2})\cdots M(s_1)|\vec{c}\rangle/P(\vec{s},\vec{c}). \tag{9}$$

To generate the ensemble Ω we use the Metropolis algorithm to update $\vec{s}$ and $\vec{c}$ alternately. We first fix the nucleon configuration $\vec{c}$ and update the auxiliary fields $\vec{s}$. Starting from the rightmost time slice s_1, we update $s_1,\ldots,s_{L_t}$ successively, as detailed in Supplemental Material [20].

After updating $\vec{s}$, we then update the nucleon configuration $\vec{c}$. To that end, we randomly choose a nucleon i and move it to one of its neighboring sites

$$c_i = \{\boldsymbol{n}_i,\sigma_i,\tau_i\} \to c_i' = \{\boldsymbol{n}_i',\sigma_i,\tau_i\}, \tag{10}$$

or flip its spin,

$$c_i = \{\boldsymbol{n}_i,\sigma_i,\tau_i\} \to c_i' = \{\boldsymbol{n}_i,-\sigma_i,\tau_i\}. \tag{11}$$

The corresponding new nucleon configuration $\vec{c}'$ is accepted if

$$P(\vec{s},\vec{c}')/P(\vec{s},\vec{c}) > r' \tag{12}$$

with $0 \le r' < 1$ a random number. Because in the $\vec{c}$ update only one nucleon is moved or spin flipped at a time, the successive configurations are correlated. Only when all nucleons have been updated do we obtain statistically independent configurations. For calculations described here, we found that about $16\vec{c}$ updates for every $\vec{s}$ update produced the optimal sampling efficiency.

At low temperatures the signal in Eq. (2) may be overwhelmed by stochastic noise due to the notorious sign problem, i.e., to the almost complete cancellation between positive and negative amplitudes. In auxiliary-field simulations with attractive pairing interactions, the sign problem is held in check by pairing symmetries. For the case of spin pairing, this means that for any nucleon with quantum numbers $(\boldsymbol{n}, \sigma, \tau)$, we can find another nucleon with $(\boldsymbol{n}, -\sigma, \tau)$. As the transfer matrix in Eq. (6) is spin independent, the pairing symmetry is preserved irrespective of the auxiliary fields. A similar pairing symmetry also holds for isospin pairing, with τ and $-\tau$. These pairing symmetries produce single-nucleon amplitude matrices with eigenvalues that come in complex conjugate pairs, such that the corresponding matrix determinants remain positive.

In the PTA, the nucleon positions and indices are allowed to explore unpaired configurations and could spoil the protection from sign oscillations provided by pairing symmetries. Indeed, this possibility is one reason why the method had not been considered earlier, and why grand-canonical calculations have instead been used for the thermodynamics of nuclear systems as well as ultracold atoms [39,40]. Fortunately, we find that this issue is not realized here. For all temperatures considered in this Letter, we find that the sign problem is rather mild, as the positive sign configurations have stronger amplitudes due to the attractive pairing interactions. However, the sign problem will eventually reemerge for temperatures very low compared to the Fermi energy. For interactions without pairing symmetries, the sign problem will be far more severe and appear even in auxiliary-field Monte Carlo calculations without pinholes.

For the values of A, V, and L_t of interest in this work, the computational scaling of the PTA is A^2VL_t, while that for the grand-canonical algorithm described in Ref. [41] is AV^2L_t. Details of the computational scaling analysis can be found in Supplemental Material [20]. The cost savings of the PTA is a factor of V/A, and the speed up factor associated with the PTA will be as large as one thousand, depending on the lattice spacing and particle density.

Next, we discuss the measurement of the observables. While the energies and density correlation functions can be directly measured by inserting the corresponding operators in the middle time step as in Eq. (8), we still need to design efficient algorithms for computing intensive variables, e.g., chemical potential μ or pressure p. This contrasts with grand-canonical ensemble calculations where the chemical potential is given as an external constraint.

In classical thermodynamics simulations, the Widom insertion method (WIM) [42] is used to determine the statistical mechanical properties [43,44]. In the WIM we freeze the motion of the molecules and insert a test particle to the system and measure the free-energy difference, from which the chemical potential can be determined. The advantage of the WIM is that we do not need the total free energy, which would require an evaluation of the partition function. In the PTA we encounter a similar problem. The absolute free energy can only be inferred with an integration of the energy from absolute zero, which induces large uncertainties. To solve this problem, we adapt the WIM to the quantum lattice simulations, with the test particles substituted by fermionic particles or holes in the system.

For every configuration $\vec{c}$ generated in the PTA, we calculate the expectation values associated with adding one nucleon or removing one nucleon. We define

$$\begin{aligned}\mathcal{B}_1 &= \sum_{c'} \langle \vec{c} \cup c' | M(s_{n_t}) \cdots M(s_1) | \vec{c} \cup c' \rangle / P(\vec{s}, \vec{c}), \\ \mathcal{B}_{-1} &= \sum_{i} \langle \vec{c} \backslash c_i | M(s_{n_t}) \cdots M(s_1) | \vec{c} \backslash c_i \rangle / P(\vec{s}, \vec{c}),\end{aligned} \tag{13}$$

where the summation over c' runs over all single-particle quantum numbers and the summation over i runs over all existing particles. $P(\vec{s}, \vec{c})$ is the probability given in Eq. (7). The extra free energy of inserting or removing one particle is given by

$$F(A \pm 1) - F(A) = -T \ln \left[\frac{\langle \mathcal{B}_{\pm 1} \rangle_\Omega}{(A \pm 1)!} \right]. \tag{14}$$

Using the symmetric difference, we have

$$\mu = [F(A+1) - F(A-1)]/2 = \frac{T}{2} \ln \left[A(A+1) \frac{\langle \mathcal{B}_{-1} \rangle_\Omega}{\langle \mathcal{B}_1 \rangle_\Omega} \right]. \tag{15}$$

In the PTA the summations in Eq. (13) can be calculated using random sampling. For $\mathcal{B}_1$ we insert a nucleon with random spin and location and propagate it through all time slices, while for $\mathcal{B}_{-1}$ we simply remove one of the existing nucleon. As only one particle is inserted or removed in each measurement, we find this algorithm very efficient and precise in calculating the chemical potential μ. Subsequently, we determine the pressure p by integrating the Gibbs-Duhem equation, $dp = \rho d\mu$, starting from the vacuum with $p = 0$, $\rho = 0$.

As the long-range Coulomb interaction is ill defined in the thermodynamic limit without screening, it is standard practice to remove the Coulomb force from nuclear matter calculations. We note that in actual heavy-ion collisions the Coulomb interaction can be important, and so the comparison with Coulomb-removed nuclear matter is not entirely straightforward. We first focus on the nuclear equation of state at nonzero temperatures, which is important for describing the evolution and dynamics of core-collapse supernovae [45], neutron star cooling [46], neutron star mergers [47], and heavy-ion collisions [48]. We then

consider nuclear clustering as a function of density and temperature.

In this work we perform simulations on $L^3 = 4^3, 5^3, 6^3$ cubic lattice with up to 144 nucleons and a spatial lattice spacing $a = 1/150$ MeV$^{-1} \approx 1.32$ fm, such that the corresponding momentum cutoff is $\Lambda = \pi/a \approx 471$ MeV. The temporal lattice spacing is taken to be $a_t = 1/2000$ MeV^{-1}. For these calculations we use the pionless effective field theory Hamiltonian introduced in Ref. [49], consisting of two- and three-body contact interactions which reproduce the binding energy and charge distribution of many light and medium-mass nuclei. While this is a simple leading-order theory and the results are only a first step towards higher-order calculations in chiral effective field theory, our simplified calculation has the important dual purpose of making our discussion of the PTA accessible to a broader audience for potential applications to the thermodynamics of condensed matter systems and ultracold atoms.

We impose twisted boundary conditions along the coordinate directions, which means that each nucleon momentum component p_i must equal $\theta_i/L + 2\pi n_i/L$ for our chosen twist angle θ_i and some integer n_i. As detailed in Supplemental Material [20], we average each observable over all possible twist angles by Monte Carlo sampling. As others have found [50–52], twist averaging significantly accelerates the convergence to the thermodynamic limit.

In Fig. 1 we present the calculated chemical potential and pressure isotherms for $L^3 = 6^3$. Each point represents a separate simulation. The temperature T covers the range from 10 to 20 MeV and densities from 0.0080 fm^{-3} to 0.20 fm^{-3}. The statistical errors are very small, less than 0.02 MeV for μ and less than 0.002 MeV/fm^3 for p. These are too small to be clearly visible in Fig. 1 and are not shown. The liquid-vapor coexistence line is determined through the Maxwell construction of each isotherm and depicted as a solid black line in Fig. 1. The liquid-vapor critical point is then located by solving the equations $d\mu/d\rho = d^2\mu/d\rho^2 = 0$. The same process is applied to the data for $L = 4^3$ and $L = 5^3$ in order to estimate the error associated with extrapolation to the thermodynamic limit.

In Table I we present the calculated critical temperature T_c, density ρ_c, and critical pressure P_c. The first error bar represents the combined uncertainty from statistics and extrapolation to the thermodynamic limit. The second error bar is the estimated systematic uncertainty associated with the contribution of omitted higher-order interactions. For completeness we also present the saturation density $\rho_{\rm sat}$ at $T = 0$ MeV and the saturation energy per nucleon $E_{\rm sat}/A$. We compare our results with the perturbative calculations using N^{3}LO chiral interactions [53] with two different momentum cutoffs. There appears to be a significant amount of dependence on the momentum cutoff, and the difference gives a rough estimate of the corresponding uncertainties. In the last column we present the empirical values deduced from the heavy-ion collision experiments [54].

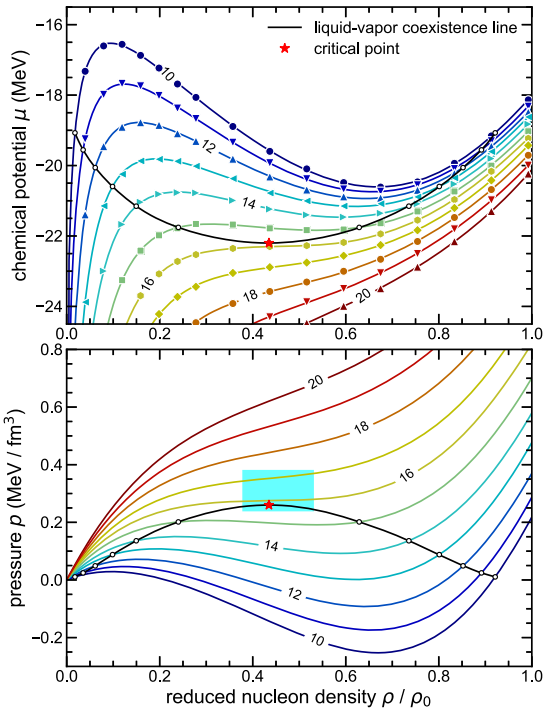

FIG. 1. Upper panel: the μ-ρ isotherms of symmetric nuclear matter computed on the lattice with $L^3 = 6^3$. The numbers on the lines are temperatures in MeV, and the temperature difference between adjacent isotherms is 1 MeV. The black line denotes the liquid-vapor coexistence line derived from Maxwell construction, and the red star marks the calculated critical point. Lower panel: the p-ρ isotherms of symmetric nuclear matter are shown for $L^3 = 6^3$. The black line denotes the liquid-vapor coexistence line, and the red star marks the calculated critical point. The cyan rectangle marks the empirical critical point extracted from heavy-ion collisions [54].

We note that while the empirical $\rho_{\rm sat}$ extracted from heavy-ion collisions is about 25% lower than the standard

TABLE I. The calculated critical temperature T_c, pressure P_c, density ρ_c, saturation density $\rho_{\rm sat}$, and energy per nucleon $E_{\rm sat}/A$. For comparison we also present the results of perturbative calculations using N^{3}LO chiral potentials, "n3lo414" and "n3lo500" correspond to cutoff momentum $\Lambda = 414$ and 500 MeV, respectively [53]. "Exp." denotes the empirical values inferred from the cluster distributions in the multifragmentation experiments [54].

	This work	n3lo414	n3lo500	Exp.
T_c (MeV)	15.80(0.32)(1.60)	17.4	19.1	17.9(4)
P_c (MeV/fm^3)	0.260(05)(30)	0.33	0.42	0.31(7)
ρ_c (fm^{-3})	0.089(04)(18)	0.066	0.072	0.06(1)
$\rho_{\rm sat}$ (fm^{-3})	0.205(08)(40)	0.171	0.174	0.132
$E_{\rm sat}/A$ (MeV)	−16.9(0.3)(1.7)	−15.79	−16.51	

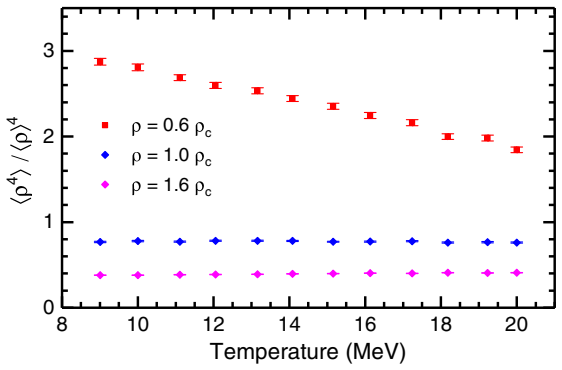

FIG. 2. The temperature dependence of the four-body density $\langle :\rho^4: \rangle$ scaled by the fourth power of the nucleon density $\langle \rho \rangle$. The results are calculated for symmetric nuclear matter on the lattice with $L^3 = 5^3$. The squares, circles, and diamonds represent total nucleon number $A = 16, 28, 40$, respectively. The corresponding nucleon densities are $\rho = 0.6\rho_c, 1.0\rho_c, 1.6\rho_c$, with $\rho_c = 0.089$ fm^{-3} the calculated critical density.

value of 0.17 fm^{-3} and our lattice ρ_{sat} is about 25% higher than 0.17 fm^{-3}, the ratios for $\rho_c/\rho_{\mathrm{sat}}$ for the two cases are in agreement with each other and also in agreement with the two N^{3}LO chiral results. This is consistent with the general expectation that small systematic errors in the density can be reduced by computing ratios of densities.

Nuclear clustering is another important phenomenon essential to our understanding of the phase diagram of nuclear matter and multifragmentation in heavy-ion collisions [55]. Here, we present the first study of nuclear clustering in a fully *ab initio* thermodynamics calculation. Nuclear clustering is a manifestation of strong many-body correlations which goes well beyond mean-field theory, and thus is very difficult to reproduce using most *ab initio* methods. In Fig. 2 we show the expectation values of the four-body density $\langle :\rho^4: \rangle$ for different temperatures. To build a dimensionless observable, we scale the results by the nucleon density $\langle \rho \rangle$ to the fourth power. The resulting quantity κ is a sensitive indicator of the degree of four-body clustering or alpha clustering. Here, we present the results for three different nucleon densities, which correspond to 0.6, 1.0, and 1.6 times the critical density ρ_c. For subcritical density $\rho = 0.6\rho_c$ the system is a plasma of small clusters and we found $\kappa \gg 1$. As the temperature increases the clusters begin to disintegrate and κ decreases. For the critical density $\rho = \rho_c$ and supercritical density $\rho = 1.6\rho_c$, we found negligible alpha clustering with $\kappa < 1$. Here, the thermal motion and small interparticle spacing overwhelm the tendency for clustering in such hot and dense environments. In this regime we find that alpha clustering is a monotonically decreasing function of the nucleon density, but does not depend on the temperature. Since nuclear clustering is very difficult to probe using other *ab initio* methods, it would be extremely interesting and useful to build upon this first study and investigate the density and temperature dependence of nuclear clustering in more detail with the PTA and high-quality chiral nuclear forces.

Future work will improve upon these calculations by including higher-order interactions in lattice effective field theory. With the pinhole trace algorithm, many exciting applications are possible based on first principles calculations of quantum many-body systems at nonzero temperature. This includes studies of superfluidity in symmetric and asymmetric nuclear matter, neutrino interactions in warm nuclear matter and supernova explosions, the properties of neutron stars and neutron star mergers, the temperature and density dependence of nuclear clusters, and extensions to other quantum many-body systems such as ultracold atoms and molecules.

We are grateful for discussions with Pawel Danielewicz, Christopher Gilbreth, and Bill Lynch. We acknowledge partial financial support from the Deutsche Forschungsgemeinschaft (TRR 110, "Symmetries and the Emergence of Structure in QCD"), the BMBF (Verbundprojekt 05P18PCFP1), the U.S. Department of Energy (DE-SC0018638 and DE-AC52-06NA25396), the National Science Foundation (Grant No. PHY1452635), and the Scientific and Technological Research Council of Turkey (TUBITAK Project No. 116F400). Further support was provided by the Chinese Academy of Sciences (CAS) President's International Fellowship Initiative (PIFI) (Grant No. 2018DM0034) and by VolkswagenStiftung (Grant No. 93562). The computational resources were provided by the Julich Supercomputing Centre at Forschungszentrum Jülich, Oak Ridge Leadership Computing Facility, RWTH Aachen, and Michigan State University.

Note added.—Through private discussions we have learned that Christopher Gilbreth is independently working on methods similar to the pinhole trace algorithm.

[1] S. R. Stroberg, A. Calci, H. Hergert, J. D. Holt, S. K. Bogner, R. Roth, and A. Schwenk, Phys. Rev. Lett. **118**, 032502 (2017).
[2] M. Piarulli, A. Baroni, L. Girlanda, A. Kievsky, A. Lovato, E. Lusk, L. E. Marcucci, S. C. Pieper, R. Schiavilla, M. Viviani, and R. B. Wiringa, Phys. Rev. Lett. **120**, 052503 (2018).
[3] D. Lonardoni, J. Carlson, S. Gandolfi, J. E. Lynn, K. E. Schmidt, A. Schwenk, and X. B. Wang, Phys. Rev. Lett. **120**, 122502 (2018).
[4] P. Gysbers, G. Hagen, J. D. Holt, G. R. Jansen, T. D. Morris, P. Navratil, T. Papenbrock, S. Quaglioni, A. Schwenk, S. R. Stroberg, and K. A. Wendt, Nat. Phys. **15**, 428 (2019).
[5] N. A. Smirnova, B. R. Barrett, Y. Kim, I. J. Shin, A. M. Shirokov, E. Dikmen, P. Maris, and J. P. Vary, Phys. Rev. C **100**, 054329 (2019).
[6] L. Contessi, A. Lovato, F. Pederiva, A. Roggero, J. Kirscher, and U. van Kolck, Phys. Lett. B **772**, 839 (2017).

[7] E. Epelbaum, H. W. Hammer, and U.-G. Meißner, Rev. Mod. Phys. **81**, 1773 (2009).
[8] M. Baldo and L. S. Ferreira, Phys. Rev. C **59**, 682 (1999).
[9] J. W. Holt, N. Kaiser, and W. Weise, Prog. Part. Nucl. Phys. **73**, 35 (2013).
[10] V. Soma and P. Bozek, Phys. Rev. C **80**, 025803 (2009).
[11] A. Carbone, A. Polls, and A. Rios, Phys. Rev. C **98**, 025804 (2018).
[12] A. Carbone and A. Schwenk, Phys. Rev. C **100**, 025805 (2019).
[13] A. Carbone, Phys. Rev. Research **2**, 023227 (2020).
[14] H. M. Müller, S. E. Koonin, R. Seki, and U. van Kolck, Phys. Rev. C **61**, 044320 (2000).
[15] D. Lee, B. Borasoy, and T. Schäfer, Phys. Rev. C **70**, 014007 (2004).
[16] C. N. Gilbreth, S. Jensen, and Y. Alhassid, arXiv:1907.10596.
[17] Y. Alhassid, C. N. Gilbreth, and G. F. Bertsch, Phys. Rev. Lett. **113**, 262503 (2014).
[18] D. Lee, Prog. Part. Nucl. Phys. **63**, 117 (2009).
[19] T. A. Lähde and U.-G. Meißner, *Nuclear Lattice Effective Field Theory: An Introduction*, Lecture Notes in Physics Vol. 957 (Springer, New York, 2019).
[20] See Supplemental Material at http://link.aps.org/supplemental/10.1103/PhysRevLett.125.192502 for details of the lattice Hamiltonian, auxiliary-field formalism, auxiliary-field updates, computational scaling, autocorrelation and sign problem, Widom insertion method, backbending of isotherms, finite volume effects, and interpolation and error analysis, which includes Refs. [21–37].
[21] L. Contessi, A. Lovato, F. Pederiva, A. Roggero, J. Kirscher, and U. van Kolck, Phys. Lett. B **772**, 839 (2017).
[22] S. Elhatisari, N. Li, A. Rokash, J. M. Alarcn, D. Du, N. Klein, B. N. Lu, U. G. Meiner, E. Epelbaum, H. Krebs, T. A. Lähde, D. Lee, and G. Rupak, Phys. Rev. Lett. **117**, 132501 (2016).
[23] A. Rokash, E. Epelbaum, H. Krebs, and D. Lee, Phys. Rev. Lett. **118**, 232502 (2017).
[24] C. Körber, E. Berkowitz, and T. Luu, Europhys. Lett. **119**, 60006 (2017).
[25] M. M. Forbes, S. Gandolfi, and A. Gezerlis, Phys. Rev. Lett. **106**, 235303 (2011).
[26] J. Carlson, Sefano Gandolfi, Kevin E. Schmidt, and Shiwei Zhang, Phys. Rev. A **84**, 061602(R) (2011).
[27] N. Byers and C. N. Yang, Phys. Rev. Lett. **7**, 46 (1961).
[28] E. Y. Loh, Jr. and D. K. Campbell, Synth. Met. **27**, A499 (1988).
[29] R. Valenti, C. Gros, P. J. Hirschfeld, and W. Stephan, Phys. Rev. B **44**, 13203 (1991).
[30] C. Gros, Z. Phys. B **86**, 359 (1992).
[31] J. Tinka Gammel, D. K. Campbell, and E. Y. Loh, Jr., Synth. Met. **57**, 4437 (1993).
[32] C. Gros, Phys. Rev. B **53**, 6865 (1996).
[33] Paulo F. Bedaque, Phys. Lett. B **593**, 82 (2004).
[34] G. M. Divitiis, R. Petronzio, and N. Tantalo, Phys. Lett. B **595**, 408 (2004).
[35] Paulo F. Bedaque and Jiunn-Wei Chen, Phys. Lett. B **616**, 208 (2005).
[36] C. T. Sachrajda and G. Villadoro, Phys. Lett. B **609**, 73 (2005).
[37] C. Körber and T. Luu, Phys. Rev. C **93**, 054002 (2016).
[38] S. Elhatisari, E. Epelbaum, H. Krebs, T. A. Lähde, D. Lee, N. Li, B. N. Lu, U.-G. Meißner, and G. Rupak, Phys. Rev. Lett. **119**, 222505 (2017).
[39] A. Bulgac, J. E. Drut, and P. Magierski, Phys. Rev. Lett. **96**, 090404 (2006).
[40] A. Bulgac, J. E. Drut, and P. Magierski, Phys. Rev. A **78**, 023625 (2008).
[41] R. Blankenbecler, D. J. Scalapino, and R. L. Sugar, Phys. Rev. D **24**, 2278 (1981).
[42] B. Widom, J. Chem. Phys. **39**, 2808 (1963).
[43] K. Binder, Rep. Prog. Phys. **60**, 487 (1997).
[44] R. P. A. Dullens, Mol. Phys. **103**, 3195 (2005).
[45] H. Togashi, K. Nakazato, Y. Takehara, S. Yamamuro, H. Suzuki, and M. Takanobe, Nucl. Phys. **A961**, 78 (2017).
[46] D. Page, J. M. Lattimer, M. Prakash, and A. W. Steiner, Astrophys. J. Suppl. **155**, 623 (2004).
[47] E. R. Most, L. J. Papenfort, V. Dexheimer, M. Hanauske, S. Schramm, H. Stöcker, and L. Rezzolla, Phys. Rev. Lett. **122**, 061101 (2019).
[48] C. B. Das, S. Das Gupta, W. G. Lynch, A. Z. Mekjian, and M. B. Tsang, Phys. Rep. **406**, 1 (2005).
[49] B. N. Lu, N. Li, S. Elhatisari, D. Lee, E. Epelbaum, and U.-G. Meißner, Phys. Lett. B **797**, 134863 (2019).
[50] C. Lin, F.-H. Zong, and D. M. Ceperley, Phys. Rev. E **64**, 016702 (2001).
[51] G. Hagen, T. Papenbrock, A. Ekström, K. A. Wendt, G. Baardsen, S. Gandolfi, M. Hjorth-Jensen, and C. J. Horowitz, Phys. Rev. C **89**, 014319 (2014).
[52] B. Schuetrumpf, W. Nazarewicz, and P.-G. Reinhard, Phys. Rev. C **93**, 054304 (2016).
[53] C. Wellenhofer, J. W. Holt, N. Kaiser, and W. Weise, Phys. Rev. C **89**, 064009 (2014).
[54] J. B. Elliott, P. T. Lake, L. G. Moretto, and L. Phair, Phys. Rev. C **87**, 054622 (2013).
[55] A. Ono, Prog. Part. Nucl. Phys. **105**, 139 (2019).